On the formation of copper nanoparticles in nanocluster aggregation source

Dutka, Mikhail V.; Turkin, Anatoliy A.; Vainchtein, David I.; De Hosson, Jeff Th. M.

Published in:
Journal of Vacuum Science & Technology A

DOI:
10.1116/1.4917002

Publication date:
2015

On the formation of copper nanoparticles in nanocluster aggregation source

Mikhail V. Dutka, Anatoliy A. Turkin, David I. Vainchtein, and Jeff Th. M. De Hosson

Citation: Journal of Vacuum Science & Technology A **33**, 031509 (2015); doi: 10.1116/1.4917002
View online: https://doi.org/10.1116/1.4917002
View Table of Contents: http://avs.scitation.org/toc/jva/33/3
Published by the American Vacuum Society

On the formation of copper nanoparticles in nanocluster aggregation source

Mikhail V. Dutka
Department of Applied Physics, Zernike Institute for Advances Materials, University of Groningen, Nijenborgh 4, 9747 AG Groningen, The Netherlands

Anatoliy A. Turkin
National Science Center, "Kharkiv Institute of Physics and Technology," Akademichna str. 1, UA-61108 Kharkiv, Ukraine

David I. Vainchtein and Jeff Th. M. De Hosson[a)]
Department of Applied Physics, Zernike Institute for Advances Materials, University of Groningen, Nijenborgh 4, 9747 AG Groningen, The Netherlands

(Received 28 December 2014; accepted 24 March 2015; published 7 April 2015)

The influence of pressure and type of inert gas (Ar and Kr) on the morphology and size distribution of nanoparticles produced in a nanocluster source is studied experimentally. The experimental data are used to validate the model of cluster formation from a supersaturated atomic vapor in an inert buffer gas, which has been developed in our previous paper. The model predictions are in accordance with the experimental findings. © *2015 American Vacuum Society*.
[http://dx.doi.org/10.1116/1.4917002]

I. INTRODUCTION

The increasing interest in the production of nanoclusters and nanoparticles of a certain size is driven by the remarkable variations in electrical, optical, and magnetic properties that occur as one down size from a bulk to a particle of material consisting of a countable number of atoms.[1] The term *nanoparticle* was commonly used already in the early 1990s together with the related concepts, *nanoscaled* or *nanosized* particle. Before that period rather general terms, such as *submicron* and *ultrafine* particles, were used. Nowadays, typically, the term *nanocluster* refer to species composed of 1000 atoms or less (large molecular clusters[2]), nanoparticles to entities with one or more characteristic dimensions less than 100 nm, and aggregates as interconnected networks of nanoparticles.[3] In the following, the terms *nanocluster* and *nanoparticle* we will use interchangeably, where this will not lead to misunderstanding. Size-dependent characteristics open a possibility for tuning properties of nanoclusters and nanoparticles by precisely controlling the formation process.[4] From a technological point of view, nanoclusters and nanoparticles can be considered as a component for a new generation of nanostructured devices and materials. However, producing such materials presents its own challenges related to understanding the rules that govern their assembly and their properties.[5]

There are multiple methods for synthesis of nanoclusters and nanoparticles, including both chemical and physical methods.[6] In this paper, we consider nanoclusters production by a gas aggregation technique, where energetic atoms generated by the vaporization of the target material are cooled and condensed in a cold inert buffer gas to create the nanoclusters and nanoparticles. There are several techniques to produce a supersaturated atomic vapor that condenses into nanoclusters in the inert gas atmosphere, e.g., sputtering,[7–9] laser ablation,[10–14] pulsed[15–17] or continuous[18] arc plasma, and nanoparticle synthesis in nonthermal plasmas, both low pressure[19] and atmospheric pressure microplasmas.[20] A comprehensive review of atomic vapor creation and cluster source design is provided by Milani and Iannottain[21] (see also review article by Robertson[22] on deposition methods to grow thin films and coatings). Among gas phase methods to produce nanoparticles, the flame synthesis should be also mentioned. Today, this technique is used for production of a variety of inorganic oxides in the form of fine particles amounting to millions of tons annually.[23] Experimental, modeling, and industrial aspects of nanoparticle formation in flames can be found in a number of review papers.[24–29] Recently, the flame synthesis method has been extended to nonoxide materials.[30] Although a number of variation exist for gas-phase synthesis processes, they all have in common fundamental mechanisms of particle formation once the atomic vapor of nanocluster precursor is generated.[31,32]

In the study described in this paper, we used a magnetron sputtering source placed into an aggregation chamber with flowing buffer gas. A detailed review of magnetron sputtering techniques can be found in Refs. 33 and 34. Plasma sputtering with a magnetron provides a method for vaporizing a wide range of materials.[35] The magnetron sputtering technique uses strong electric and magnetic fields to confine charged plasma particles close to the surface of the sputter target. In a magnetic field, electrons follow helical paths around magnetic field lines and undergo multiple ionizing collisions with neutral gas atoms near the target surface. The extra gas ions created as a result of these collisions lead to an increase in sputtering rate. It also means that the plasma can be sustained at a lower pressure. A particular advantage of sputtering over evaporation is that it does not involve complications related to target heating. Sputtered atoms are predominantly neutral (only from 10^{-4} to 10^{-3} atoms are ionized[7,36,37]) and so are unaffected by the magnetic trap. According to Haberland[8] in magnetron based gas aggregation sources, a high percentage (20%–80%) of charged

[a)]Electronic mail: j.t.m.de.hosson@rug.nl

clusters can be obtained because of charge transfer processes in the plasma region. However, in Ref. 38, a rather low cluster ion current was measured with a quadrupole mass filter in a nanocluster source similar to that used in our study; the estimated fraction of charged silver nanoclusters was in the range of a few percent. It seems that the fraction of charged nanoparticles depends on parameters of the magnetron sputtering source and the geometry of the aggregation chamber. This question needs more investigation.

Nanoclusters nucleate from the atomic vapor and grow in the aggregation chamber until the mixture of gas and nanoclusters/nanoparticles is released through an aperture into a surrounding vacuum chamber. By changing the experimental conditions the particle morphology and the particle size distribution (PSD) can be controlled to produce nanoparticles with optimal properties. Nucleation and growth of nanoparticles are affected by several parameters, such as the temperature, the residence time of particles in the aggregation chamber, and the ratio of the material gas to the inert gas. Frequently, the effect of experimental conditions on nanoclusters formation is difficult to predict, and certain properties of nanoclusters cannot be measured directly. For this reason, theoretical calculations and computer simulation play significant role in the nanocluster research and help to optimize the operating conditions to create nanoclusters with desired size distribution and properties. Commonly known computational methods such as molecular dynamics and Monte Carlo simulation are used for modeling and prediction of effects of experimental conditions on PSD.[39–41] However, Monte Carlo simulations are limited to rather small number of atoms in clusters due to significant computational requirements. In our previous paper,[42] we have developed a mean-field description of PSD evolution via cluster coagulation driven by Brownian motion in the aggregation chamber. The simulation results have shown a good agreement with the experimental data on the particle size distribution of copper nanoparticles formed in NC200-UHV nanocluster source with Ar as a buffer gas at a pressure of 40 Pa.

In this paper, we study experimentally the influence of pressure and type of inert gas (Ar and Kr) on the morphology and the size distribution of produced nanoclusters. The experimental data are compared to simulation results obtained with the model developed in our previous work.[42]

II. EXPERIMENTAL SETUP AND METHODS

The clusters were produced with a NC200-UHV nanocluster aggregation source from Oxford Applied Research. Figure 1 gives a schematic view of the ultrahigh vacuum system used in this work. It consists of several basic parts: a gas aggregation chamber, a deposition chamber, an intermediate chamber, and an airlock. A small aperture (3 mm in this work) separates the aggregation and deposition chambers from one another.

A magnetron sputtering device, located in the aggregation chamber, is used as a source of atoms. An inert buffer gas fed to the magnetron is ionized partly by a DC voltage applied between the target and the magnetron cover and serves as a sputtering gas. The inert gas also transports atoms and clusters along the aggregation chamber toward the aperture. Length of the aggregation region can be varied from 50 to 200 mm by changing the position of the magnetron. This design concept was adopted from Haberland *et al.*,[7] who first applied the sputter discharge technique in a cluster source instead of the conventional thermal evaporation. The intermediate chamber contains a saddle field fast atom bombardment gun that could be used for cleaning the substrate before deposition.[43] The airlock has a separate pumping system, consisted of a turbomolecular pump and a diaphragm pump, which allows quick sample change.

Due to a high atomic flux from the cluster source, a suitable deposition time for all the samples was 15 s. To achieve high reproducibility at these short times, the deposition process has been made fully automated. For this purpose, a personal computer (PC)-based control system was built consisting of National Instruments interface cards and LABVIEW software, a flow controller, pressure gauges, and a Glassman Europe

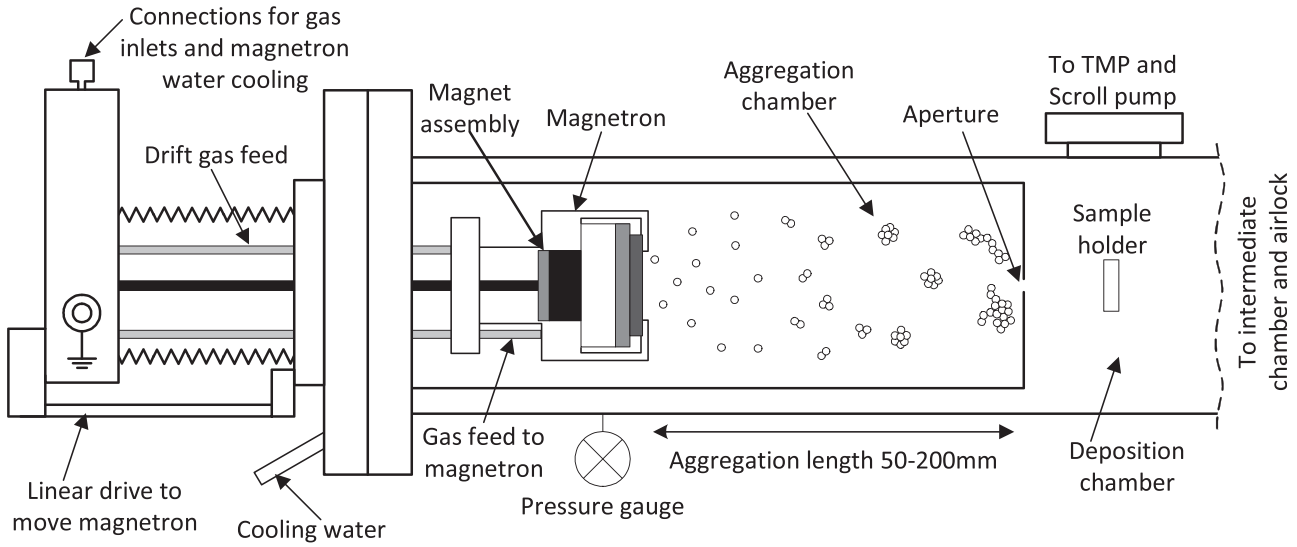

FIG. 1. Schematic view of the nanocluster aggregation source.

TABLE I. Experimental conditions for nanocluster formation.

Type of buffer gas	Pressure, P_g (Pa)	Gas flow rate, Q_g, (sccm)	Copper yield, Q_{Cu}, (mg/h)	Magnetron voltage (V)	Magnetron current (A)	Magnetic field above the target erosion zone (T)
Ar	20	8.4	358	370	0.21	1.18
Ar	40	16.8	270	360	0.21	1.18
Kr	20	8.4	310	375	0.21	1.18
Kr	40	16.8	186	365	0.21	1.18

magnetron power supply. In our installation, an amount of material removed from the target, or a sputter yield, is dependent on the pressure inside of the aggregation chamber as well as on the type of inert gas. For reliable comparison of samples obtained at different conditions, it is essential to know the sputter yield. For this reason, weight loss of target was measured after hour-long deposition for every experimental condition and was taken into account for modeling.

Metal atoms were sputtered from a pure copper target and condensed into clusters within the aggregation region filled with an inert gas. Experiments were performed with two types of gas, Ar and Kr, and at two different pressures, 20 and 40 Pa (Table I).

The choice of the specific gas was made according to the elastic-collision theory,[44] which suggests that for efficient momentum transfer, the atomic weight of the sputtering gas should be close to the atomic weight of the target. Note that the gas pressure change leads to changes in copper yield from the target (Table I).

The clusters were deposited onto a 20 nm thick amorphous carbon film, supported by Cu grid for analysis in a JEOL 2010F transmission electron microscope (TEM) operated at 200 kV. TEM images of each sample have been taken at two magnifications. The lower magnification images (×100 000) were used to evaluate a surface density of Cu nanoparticles, while morphology of the nanoparticles was determined from the higher magnification images (×300 000). This approach helped to characterize nanoparticles with a high accuracy by analyzing either large number of objects or high resolution images when necessary. A sufficient number of images were acquired to allow the evaluation of more than 100 individual aggregates per sample.

Image preprocessing and analysis were performed using MATLAB software package following closely the procedures described in the literature.[45–47] Aggregates that touch edges of images were excluded from the analysis, as there were aggregates having too low contrast to the background. Obtained binary images were analyzed using a custom written MATLAB code. This code allows us to determine the projected area of agglomerate, its maximum projected length L, and width W in the direction perpendicular to L.

III. EXPERIMENTAL RESULTS

In this work, we examine the samples obtained at four different conditions mentioned earlier. To study the cluster formation process, we evaluate the size distribution as a function of distance from the target. The TEM grids were placed inside the aggregation tube, close to its axis at distances of 50, 80, 120, and 170 mm from the target. At a distance of 50 mm for all experimental conditions, the deposition rate was very high, resulting in a film with densely packed nanoclusters [Fig. 2(a)]. Therefore, such samples were not possible to analyze using image processing algorithms.

Further downstream, at the distance of 80 mm, well defined separate clusters were formed. Although at certain conditions many small clusters (less than 2 nm), almost indistinguishable from the background, were also seen on the substrate [Fig. 2(b)]. The presence of these small clusters was confirmed by high-resolution TEM images and energy-dispersive x-ray spectroscopy. For the purity of experiment, all the samples collected at distances of 50 and 80 mm were rejected for the further image analysis as well as for the comparison with model calculations.

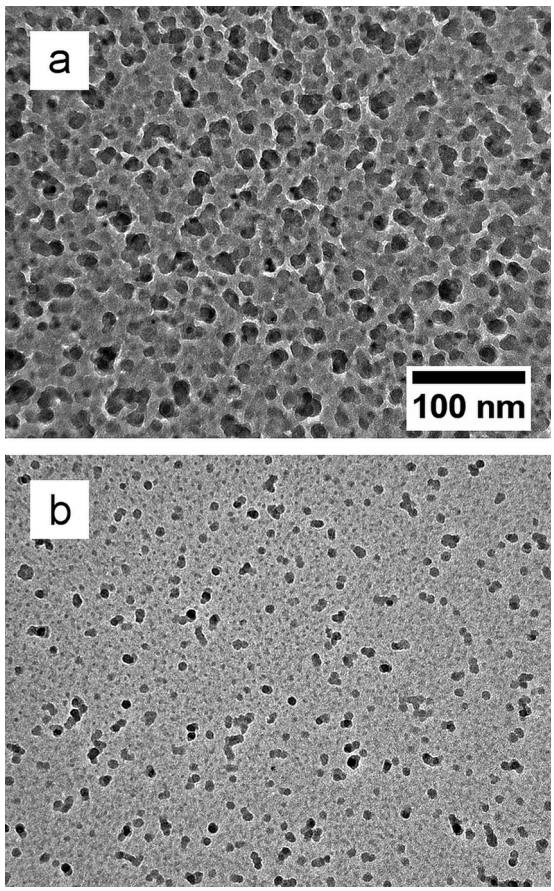

FIG. 2. Example of samples not suitable for image processing: (a) film of clusters formed at the distance of 50 mm from the target and (b) well defined clusters with many small particles between them (collected at 80 mm). Such samples were rejected from further analysis.

TEM images of collected nanoparticles are presented in Fig. 3. As can be seen for both samples using Ar gas, at 120 mm, the deposited particles have a compact shape close to spherical one with the mean diameter about 8 nm. Whereas at 170 mm, nanoparticles formed at the pressure of 20 Pa still have compact shape, the ones formed at 40 Pa are undoubtedly dendritelike with maximum sizes in the range of 50 nm. The other noticeable difference between these two samples is the surface density, which is much higher for 20 Pa at 120 mm, but lower at 170 mm. The particles formed using Kr gas are larger comparing to the ones formed with Ar gas, and their mean diameter is about 12 nm. However, the morphology did not change significantly, and only the surface density becomes lower downstream.

Our study focuses on nanoparticle formation inside the aggregation tube in order to understand the processes governing particle growth and evolution of PSD. Although in a practical application of the nanocluster source, the substrate is placed after the aperture, so the deposition actually occurs outside the aggregation tube.

Figure 3 (lower row) shows the TEM images of samples collected after the aperture. At the same experimental conditions, there is a significant difference between populations of nanoparticles collected 30 mm before the aperture and after it. This effect is caused by the flow of buffer gas with suspended nanoparticles through the aperture. However, aggregates of nanoparticles collected after the aperture consist of primary particles of about the same diameter as the nanoparticles before the aperture. Additional experiments with shorter deposition times or lower deposition rates, to avoid overlapping of particles on the substrate, might clarify this observation; however, this question lies outside of the scope of this work.

IV. MODEL OF PSD EVOLUTION

In this section, the model of nanocluster formation developed in Ref. 42 is briefly outlined. In Sec. V, the model is applied to calculate PSD close to the axis of the aggregation tube for the experimental conditions discussed above. The particle size distribution is defined by densities of clusters of all sizes $C_k(x)$, where $k > 1$ is the number of atoms in clusters and x is the coordinate along the aggregation tube.

To describe the evolution of PSD, we use a mean-field approach based on the Smoluchowsky coagulation equation[48] for the growth of clusters by successive mergers. The following assumptions are adopted in the model:

(1) Gas of metal atoms is unstable with respect to nucleation and coagulation of clusters.
(2) Except during collisions, the interactions among clusters are negligible.
(3) No fragmentation of colliding clusters occurs.
(4) No thermal dissolution of clusters by monomer evaporation from the cluster surface.
(5) Clusters suspended in the buffer gas undergo random walks and drift downstream with the velocity V of the buffer gas flow.

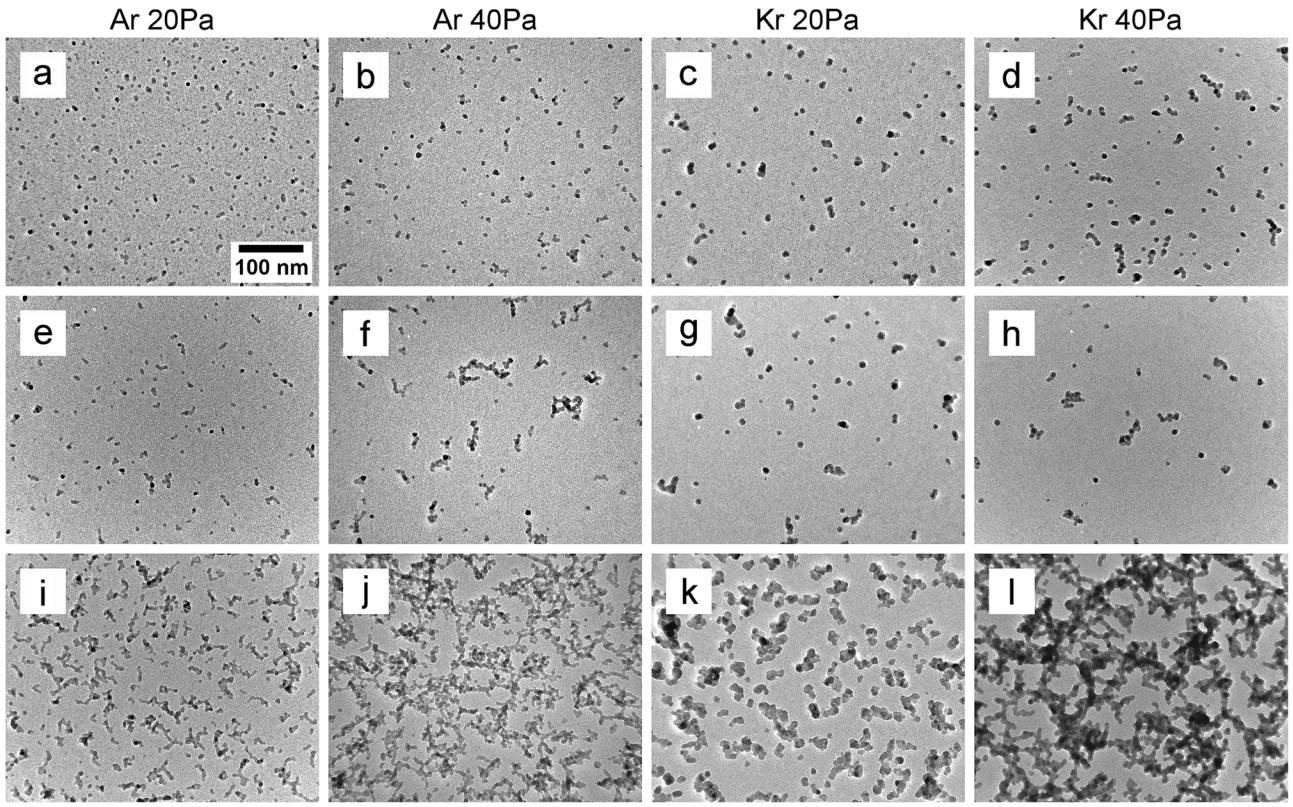

FIG. 3. TEM images of Cu clusters collected inside the aggregation tube close to its axis during deposition time 15 s at the distance of 120 mm [(a)–(d)], 170 [(e) and (f)] from the target, and after the aperture [(i)–(l)]. The scale bar is the same for all images.

TABLE II. Parameters used for simulation of nanocluster formation.

Length of aggregation chamber, L (mm)	200
Radius of aggregation chamber, R (mm)	50
Aperture diameter, a (mm)	3
Temperature, T (K)	300
Sticking coefficient for the dimer formation in Ar, η_{11}	$3.9 \times 10^{-7} P_{\mathrm{Ar}}$
Sticking coefficient for the dimer formation in Kr, η_{11}	$3.0 \times 10^{-7} P_{\mathrm{Kr}}$
Fractal dimension of large clusters, D_f^{∞}	1.8
Maximum number of atoms in a cluster with $D_f(k) = 3$, k_0	1100
Parameter k_a, Eq. (19)	1.1
Parameter α_a, Eq. (19)	1.6

Small clusters formed by coagulations have a shape close to the spherical one. When clusters become sufficiently large, the time of thermal sintering of colliding clusters is longer than the mean time between successive collisions, and particles grow as dendrite- or fractal-shaped aggregates with morphology that can only be characterized at the statistical level by the fractal dimension D_f.[32,49,50] Brasil *et al.*[51] have analyzed experimental and model results reported by several authors for the fractal dimensions of aggregates and concluded that apart from singular results most predictions fall within the range of 1.6–1.9. In the majority of studies devoted to characterization and simulations of fractal-like particles, the D_f values are evaluated assuming that aggregates consist of monodisperse primary particles. Eggersdorfer and Pratsinis[52] have generated aggregates consisting of polydisperse primary particles by various computer algorithms. It was found that polydispersity of primary particles results in more open aggregate structures with lower D_f values than the classic aggregates obtained by simulations with monodisperse primary particles. This is most notable for particle–cluster (up to 50% reduction) and to a lesser extent for cluster–cluster (up to 20% reduction) ballistic and diffusion-limited collision-generated aggregates.[52] Broadening the primary particle size distribution of aggregates decreases monotonically their D_f; for sufficiently broad primary particle distributions (geometric standard deviation >2.5), the fractal dimension reaches a value of about 1.5, regardless of the collision mechanism.[52] The modeling results concerning the influence of fractal dimension on the evolution of PSD can be found in Refs. 32 and 53.

In our model, we use a reasonable assumption that the fractal dimension depends on number of atoms k in a nanoparticle. Small nanoclusters grow spherically up to the radius $R_0 = r_{\mathrm{Cu}} \sqrt[3]{k_0}$, where k_0 is the number of atoms (see Table II). Larger nanoclusters and nanoparticles grow in the form of fractal-like aggregates. The fractal dimension of aggregates of intermediate sizes we describe by a decreasing function of cluster size k

$$D_f(k) = \begin{cases} 3 & \text{at } k \le k_0 \\ D_f^{\infty} + \left(3 - D_f^{\infty}\right)\left[1 + \left(\dfrac{k-k_0}{10k_0}\right)^2\right]^{-1} & \text{at } k > k_0, \end{cases} \tag{1}$$

where $D_f^{\infty} = \lim_{k\to\infty} D_f(k)$ is the fractal dimension of large aggregates, which is assumed to be 1.8 (Table II).

We consider the nanoparticle coagulation in the approximation of hard sphere collisions. Obviously, encounters between fractal-like aggregates are more frequent than between spherical nanoparticles with the same number of atoms. We use the following relation for the effective collision radius of fractal-like aggregates:[54,55]

$$R_c(k) = R_0 \left(\frac{k}{k_0}\right)^{1/D_f(k)} \ge r_{\mathrm{Cu}} \sqrt[3]{k}, \tag{2}$$

which is valid also for spherical nanoclusters: $R_c(k) = r_{\mathrm{Cu}} \sqrt[3]{k}$ at $k \le k_0$.

The set of equations describing the variation of PSD with the "stream-time" $\tau = x/V$ is given by

$$\frac{dC_1}{d\tau} = -V\mu(D_1)C_1 - C_1 \sum_{i=1}^{\infty} w_{i,1} C_i, \tag{3}$$

$$\frac{dC_k}{d\tau} = -V\mu(D_k)C_k + \frac{1}{2}\sum_{i=1}^{k-1} w_{i,k-i} C_i C_{k-i} - C_k \sum_{i=1}^{\infty} w_{ik} C_i, \quad k \ge 2. \tag{4}$$

The mean drift velocity of the buffer gas in the aggregation tube

$$V = \frac{k_B T Q_g}{\pi P_g R^2} \approx 0.1\,\mathrm{m/s}, \tag{5}$$

where k_B is the Boltzmann's constant, T is the temperature, Q_g is the rate of buffer gas flow, P_g is the gas pressure, and R is the radius of the aggregation tube. The parameter $\mu(D_k)$ describes nanoparticles loss to the cylindrical wall of the aggregation tube due to diffusion to macroscopic distances[42]

$$\mu(D_k) = \frac{V}{2D_k}\left(\sqrt{1 + \left(\frac{2D_k}{VR}\right)^2 {\beta_1}^2} - 1\right), \tag{6}$$

where $\beta_i = 2.2048$. The diffusion coefficient of nanoparticles of size k

$$D_k = \frac{1}{3}\sqrt{\frac{2}{\pi}}\sqrt{\frac{1}{m_g} + \frac{1}{k\,m_{\mathrm{Cu}}}}\frac{(k_B T)^{3/2}}{P_g \pi \left(r_g + r_{\mathrm{Cu}} k^{1/3}\right)^2}, \tag{7}$$

where m_{Cu} is the atomic mass of Cu and $r_{\mathrm{Cu},g}$ are the atomic radii of Cu and buffer gas atoms. This equation overestimates the mobility of fractal-like nanoparticles.[56] A more refined expression for the diffusion coefficient of fractal-like aggregates can be used

$$D_k^{\mathrm{Agg}} = \frac{1}{3}\sqrt{\frac{2}{\pi}}\sqrt{\frac{1}{m_{\mathrm{Ar}}} + \frac{1}{k\,m_{\mathrm{Cu}}}}\frac{(k_B T)^{3/2}}{P_{\mathrm{Ar}} \pi \left(r_{\mathrm{Ar}} + R_c(k)\right)^2}. \tag{8}$$

However, the simulation of PSD evolution with both coefficients produces very close results[42] because for a sufficiently

large nanoclusters ($k > 10^4$) diffusion to macroscopic distances takes more time than the residence time of nanoparticles in the aggregation chamber, $R^2/D_k > L/V$.

The boundary conditions for the set of equations is given by

$$C_1|_{x=0} = C^0_{\text{axis}}, \tag{9}$$

$$C_k|_{x=0} = 0, \quad k \geq 2, \tag{10}$$

$$C_k|_{k\to\infty} \to 0. \tag{11}$$

The starting value for monomer density C^0_{axis} is estimated from the solution of diffusion equation for monomers without coagulation

$$C^0_{\text{axis}} = \frac{32Q_{\text{Cu}}}{\pi R^2 V}\sum_{i=1}^{\infty}\frac{1}{\beta_i{}^3 J_1(\beta_i)}\left(\sqrt{1+\left(\frac{2D_1}{VR}\right)^2\beta_i{}^2}+1\right)^{-1}, \tag{12}$$

where $J_n(..)$ is the Bessel function of the order n of the first kind; $\beta_i = 2.2048, 5.5201, 8.6537,\ldots$ are the positive roots of $J_0(\beta_i) = 0$ and Q_{Cu} is the total flux of copper atoms sputtered from the target (copper yield). The total flux of copper atoms from the target was found by measuring the mass loss during target sputtering for a given period of time.

Construction of the collision kernel w_{ik} of nonspherical particles and aggregates under rather general conditions is considered in Ref. 57. In this work, we restrict ourselves to conditions specific to the nanocluster source described above. Under typical experimental conditions (Table I), the precursor Cu atoms and nanoclusters form a dilute gas mixture in argon gas $C_{\text{Ar}} \gg C^0_{\text{axis}} > C_k$, $k \geq 1$. The mean collision free path λ of argon atoms is in the range from 0.5 to 1 mm, i.e., the Knudsen number $Kn = \lambda/R_c(k) \gg 1$. Besides, even a conservative estimate of the diffusion Knudsen number Kn_D with the diffusion coefficient of fractal-like aggregates shows that

$$Kn_D = \frac{D^{\text{Agg}}_k(k)}{V_{\text{th}}(k)R_c(k)} \gg 1, \tag{13}$$

for all sizes $k < 10^7$ atoms per nanoparticle, i.e., for the nanoparticle size range studied in this work. Here,

$$V_{\text{th}}(k) = \sqrt{\frac{8k_BT}{\pi k m_{\text{Cu}}}} \tag{14}$$

is thermal velocity of nanoparticles. These mean that our experiment was performed under free-molecule conditions when nanoparticles act like large molecules traveling in straight lines (ballistically).[58] In the free-molecule limit, the

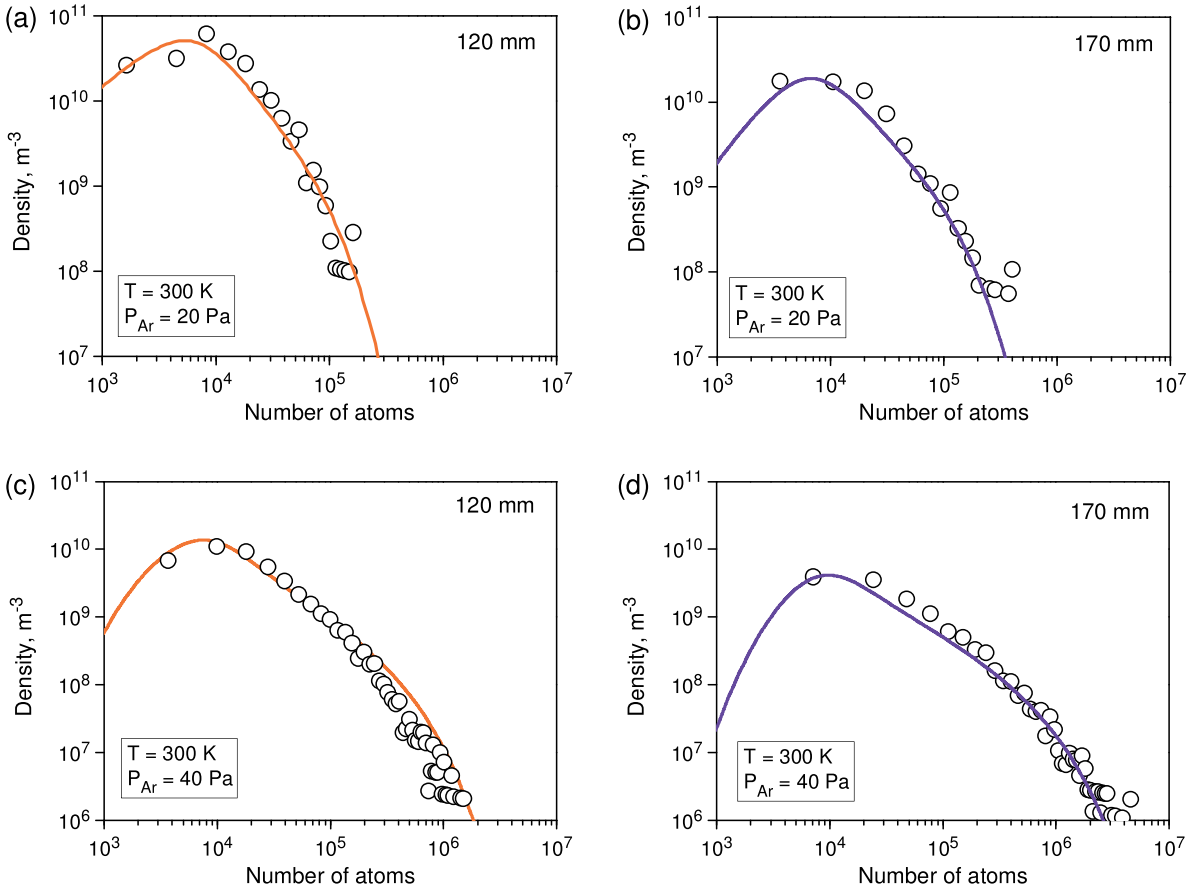

FIG. 4. (Color online) Size distribution of nanoclusters at distances 120 and 170 mm from the Cu target. Argon was used as the buffer gas. (a) and (b) Argon pressure was 20 Pa. (c) and (d) Argon pressure was 40 Pa. Symbols correspond to experimental distributions $F^{\text{exp}}_V(n)$ reconstructed from surface distributions $F_S(A)$ using Eqs. (19) and (20). The solid line shows results of modeling. Sticking coefficients $\eta_{12} = 200\eta_{11} = 7.8 \times 10^{-5}P_{\text{Ar}}$ and $\eta_{13} = 10^4\eta_{11} = 3.9 \times 10^{-3}P_{\text{Ar}}$.

coagulation kernel w_{ik}, appropriate both for small spherical nanoclusters and fractal-like aggregates, is given by[32]

$$w_{ij} = \eta_{ij}\left(R_c(i) + R_c(j)\right)^2 \sqrt{\frac{8\pi k_B T}{m_{\mathrm{Cu}}}\left(\frac{1}{i} + \frac{1}{j}\right)}, \tag{15}$$

where η_{ij} is the sticking coefficient (see below).

In Refs. 58 and 59, the validity of Eq. (15) is discussed, and an effective collision diameter that depends on the geometries of the two participating fractal-like aggregates is introduced. In particular, it was found that if the size disparity of the colliding fractal-like aggregates is large, the effective collision diameter obtained as a sum of collision radii is overestimated by about 15% at $D_f = 1.8$.[58,59] We believe that in our problem this effect plays a minor role because Cu monomers and small-sized nanoclusters are effectively removed from the coagulation process due to fast diffusion to the walls of the aggregation chamber.[42] It should be mentioned that the collision frequency is modified when particles exert forces on one another.[60] Metallic cluster may interact via long range Coulomb and van der Waals forces. Corresponding enhancement factors[61,62] can be introduced into Eq. (15), if the majority of nanoparticles would be charged. In our installation, the magnetron operates in a direct current mode. In magnetron, discharges, mainly ions of buffer gas, are present, and the ionization of sputtered atoms is very low.[7,33,36,37] At the same time, the supply of charged Cu monomers and small-sized nanoclusters in the aggregation chamber is rapidly depleted because of fast diffusion to walls[42] and a strong Coulomb interaction of nanoclusters with charges of opposite sign (note that in magnetron sputtering technique the discharge plasma is confined close to the surface of the sputter target, so no ionization takes place in the aggregation chamber). Concerning the van der Waals forces, calculations of the enhancement factor for spherical particles can be found in Ref. 62 (see also references therein). It seems that for fractal-like nanoparticles, these calculations are not valid.

What is important is that Eq. (15) contains the sticking coefficient η_{ij} because not all collisions result in cluster coalescence. The nucleation of clusters starts with formation of dimers, which is controlled by a three body collision between two copper atoms and a gas atom (the energy transfer mechanism).[39,63] An estimation of the sticking coefficient η_{11} for dimer formation is[42]

$$\eta_{11} = \frac{9\sqrt{\pi}}{2}\left(\frac{\sigma}{r_{\mathrm{Cu}}}\right)^5 \left(\frac{E_{\mathrm{rel}}}{k_B T}\right)^{-4/3} \left(\frac{\varepsilon}{k_B T}\right)^{5/6} \sqrt{\frac{1}{2} + \frac{m_{\mathrm{Cu}}}{m_g}} \frac{P_g r_{\mathrm{Cu}}^3}{k_B T}, \tag{16}$$

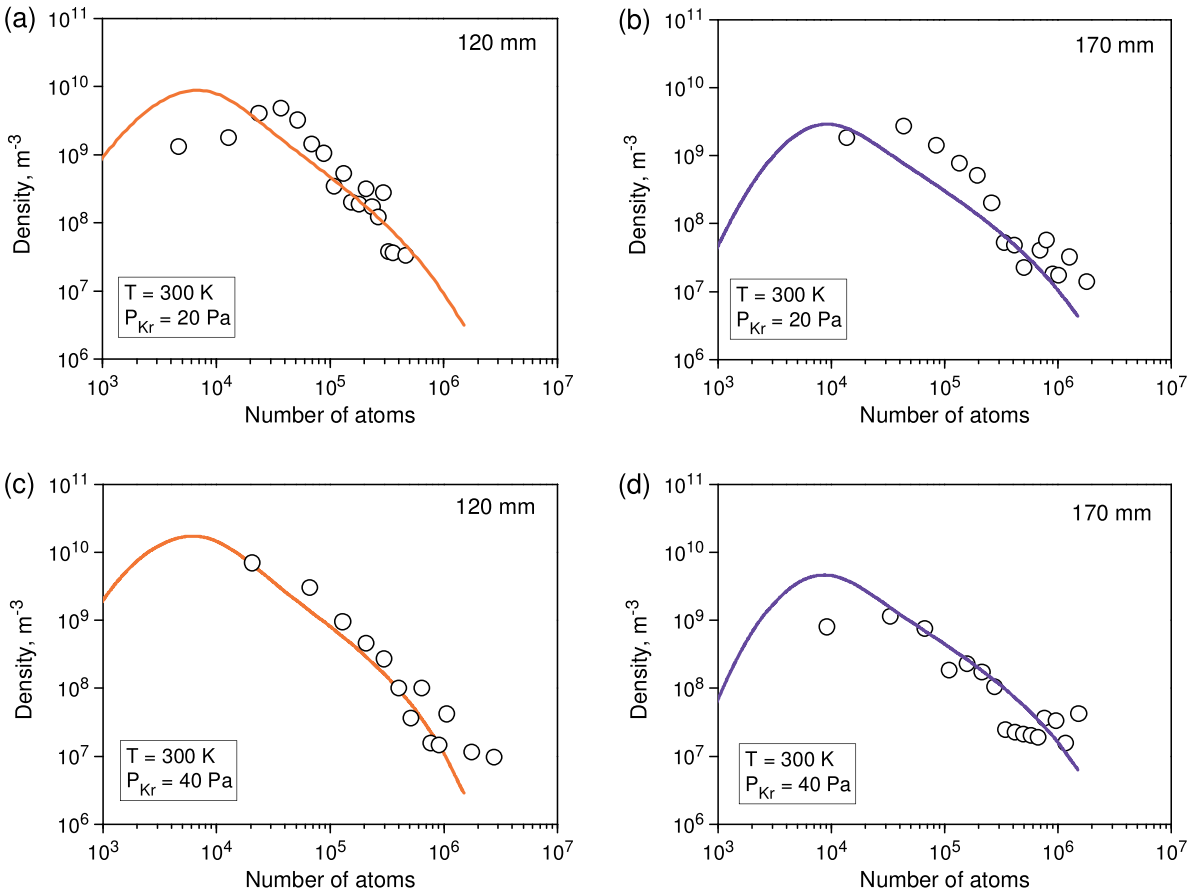

FIG. 5. (Color online) Size distribution of nanoclusters in the aggregation tube filled with krypton. (a) and (b) Krypton pressure was 20 Pa. (c) and (d) Krypton pressure was 40 Pa. Distances from the Cu target are indicated in figures. Symbols correspond to experimental distributions $F_V^{\mathrm{exp}}(n)$. The solid lines show results of modeling. Sticking coefficients $\eta_{12} = 50\eta_{11} = 1.5 \times 10^{-5} P_{\mathrm{Kr}}$ and $\eta_{13} = \eta_{22} = 1$.

where $\varepsilon = 2.03$ eV, $\sigma = 0.198$ nm and $E_{\text{rel}} \approx 3k_BT$ is the relative kinetic energy of two Cu atoms. According to Eq. (16), for the gas pressure used in this work, $\eta_{11} \ll 1$, i.e.,

$$\eta_{11} = \begin{cases} 3.9 \times 10^{-7} P_{\text{Ar}} \\ 3.0 \times 10^{-7} P_{\text{Kr}}, \end{cases} \tag{17}$$

where the pressure $P_{\text{Ar,Kr}}$ is measured in Pa units.

Modeling[42] have shown that the PSD evolution is the most sensitive to variation of sticking coefficients for clusters with sizes in the range of $2 \le i + j \le 4$. In the following, we will adjust coefficients for sizes i and j from the interval $2 < i + j \le 4$ and assume that the sticking coefficients $\eta_{ij} = 1$ for $i + j > 4$, i.e., all cluster collisions result in coagulation.

V. COMPARISON OF MODELING RESULTS WITH EXPERIMENTS

The area density of deposited cluster N_S was measured experimentally. The total volume density of cluster $N_V = \sum_{k>1} C_k$ was found from N_S using the relation

$$N_S = N_V vt, \tag{18}$$

where $t = 15$ s is the deposition time for all samples.

The nanocluster PSD $F_V^{\text{exp}}(n)$ was reconstructed from the surface distribution $F_S(A)$ over the cluster projected area A. The surface distributions of nanoclusters deposited to amorphous carbon substrates inside the aggregation tube were derived from the TEM image analysis. To relate the aggregate projected area A with the number of atoms n in it we used the following corresponding formula from Ref. 49:

$$n = k_0 k_a \left(\frac{A}{\pi r_{\text{Cu}}^2 k_0^{2/3}} \right)^{\alpha_a}, \tag{19}$$

where k_a and α_a were treated as the fitting parameters when comparing simulation results with experimental PSD. The reconstructed PSD $F_V^{\text{exp}}(n)$ is given by

$$F_V^{\text{exp}}(n) = \frac{F_S(A)}{vt} \frac{dA}{dn}. \tag{20}$$

Using parameters listed in Tables I and II, we solved Eqs. (3)–(10) numerically by the method outlined in the Appendix. The parameters k_0 and D_f^{∞} and sticking coefficients (η_{12}, η_{13}, and η_{22}) were adjusted to obtain a good agreement with measured volume density and PSD.

Comparison between experimental and model distributions is presented in Figs. 4 and 5. Figure 4 shows that the increase in Ar pressure enhances the coagulation, i.e., the distribution becomes broader. The reason is that according to Eq. (7), the cluster diffusivity decreases; hence, the cluster loss to wall reduces. In case of Kr buffer gas, this effect is not observed, probably because with Kr pressure increase the copper yield decreases substantially (Table I). Note that model distributions were calculated with the same set of parameters both for Ar and Kr, except for the sticking coefficients η_{12}, η_{13}, and η_{22} indicated in figure captions. Detailed calculation of sticking coefficients lies outside of the scope of this work, since it requires knowledge of interaction between gas atoms and clusters at the atomic level.

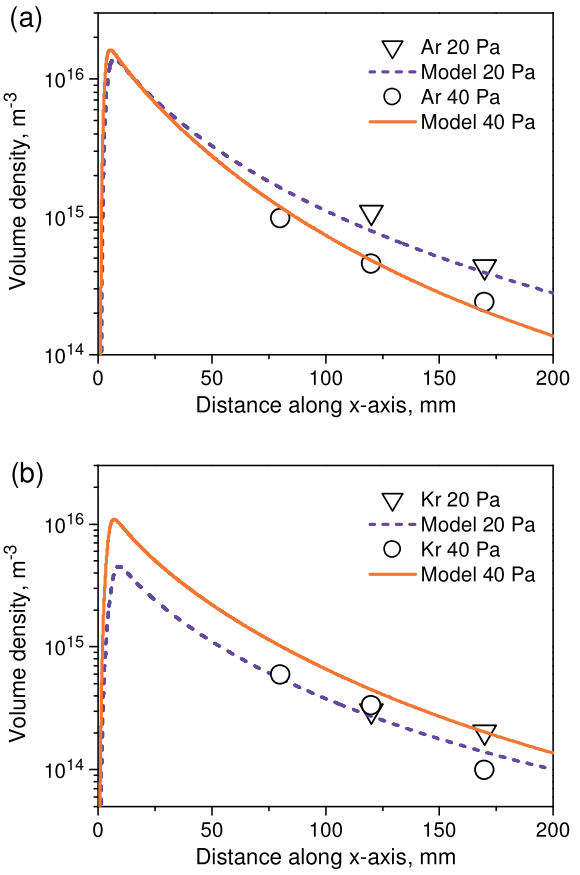

FIG. 6. (Color online) Dependence of volume density of Cu nanoparticles on the distance from the Cu target in the aggregation tube filled with argon (a) and krypton (b). Experimental data are shown by symbols.

In Fig. 6, the dependence of nanoparticle volume density on distance along the aggregation tube is compared with the volume density predicted by the model for experimental conditions studied.

VI. CONCLUSIONS

The influence of pressure and type of inert gas (Ar and Kr) on the morphology and PSD of nanoparticles produced in a nanocluster source NC200-UHV has been studied experimentally with TEM.

The experimental data were used to validate the model of cluster formation and the Smoluchowski coagulation in the inert gas, which has been formulated previously. For properly chosen parameters, a good agreement has been obtained between the experimental data and predictions of the model.

The developed model is a useful tool in planning future experiments with nanoparticles production in NC200-UHV nanocluster source and similar installations. For example, in the model, the nanoparticles PSD can be manipulated by selecting the type of target, the sputtering yield of precursor (that is controlled by the power supplied to the magnetron), the exit aperture size, the type and flow rate of inert gas, temperature in the aggregation tube, etc.

ACKNOWLEDGMENT

The Netherlands Organization for Scientific Research NWO is acknowledged for awarding a visitor's grant to one of the authors (A.A.T.).

APPENDIX: NUMERICAL METHOD

Obviously, the set of equations for PSD [Eqs. (3) and (4)] can be solved only numerically. However, this set is not suitable for practical computer calculations, since it contains too many coupled equations, e.g., more than 10^6 equations have to be solved simultaneously to track the evolution of a nanoparticle population with sizes in the range of $R < 15\,\text{nm}$. The general approach to decrease the number of equations is to approximate the initial set by a set with a controlled number of equations. Existing numerical methods are reviewed in Refs. 64–69. Here, we propose a new simple and straightforward method. We start from the observation that the set of ordinary differential equations (ODE) given by Eq. (4) is the discretized version of the integrodifferential equation for the continuous cluster size variable z

$$\frac{\partial F(z)}{\partial \tau} = -V\mu(D(z))F(z) + \int_0^{z/2} W(y, z-y)F(y) \times F(z-y)dy - F(z)\int_0^{\infty} W(y,z)F(y)dy\,. \quad \text{(A1)}$$

One can easily restore Eq. (4) from Eq. (A1) by replacing integration with the trapezoidal summation on the uniform size mesh

$$z_k = k, \quad k = 0,\,1,\,2,\,\ldots,$$
$$D_k = D(k), \quad C_k = F_k \equiv F(z_k), \quad w_{ij} = W(i,j), \quad \text{(A2)}$$

with additional requirement $F(0) = 0$. Therefore, instead of Eq. (4), we will solve the equivalent integrodifferential Eq. (A1). The idea is to calculate numerically definite integrals in the right-hand-side of Eq. (A1). To this end, we convert this equation into a new set of ODE for discrete cluster sizes on a coarse nonuniform mesh. The following relations for mesh points z_k and mesh spacings Δz_k are used:[70]

$$z_1 = 1, \quad z_k = z_{k-1} + \Delta z_k, \quad 2 \le k \le K,$$
$$\Delta z_k = \begin{cases} 1\,, & \text{at } 2 \le k \le N \\ \Delta z_{k-1}\exp(\varepsilon), & \text{at } N < k \le K, \end{cases} \quad \text{(A3)}$$

where K is large enough to meet the boundary condition $C(z_K) = 0$ to a good accuracy. Note that the mesh is uniform up to $z_N = N$ with the spacing $\Delta z = 1$. The parameter N should be sufficiently large. To be on a safe side, we use the value in the range of $N \sim 100$. For point numbers $k > N$, the spacing between mesh points increases exponentially with k, $\Delta z_k = \exp[\varepsilon(k-N)]$. The variation of mesh spacing is controlled by the positive parameter ε that should be small, $0 < \varepsilon < 1$. In calculations, we choose the end point of solution interval $z_{\max} = z_K$, N and ε. The number of ODE on the new mesh [Eq. (A3)] is estimated as

$$K \approx N + \varepsilon^{-1}\ln(\varepsilon\, z_{\max}), \quad \text{(A4)}$$

where $1 \ll N \ll z_{\max}$ and $z_{\max}^{-1} \ll \varepsilon \ll 1$. Due to coarse-graining of the numerical mesh, the number of equations can be reduced substantially (by several orders of magnitude) as compared to the initial set of discrete equations.

For the integration, we use the trapezoidal summation rule. The integral in the third term of the right-hand-side of Eq. (A1) is given by

$$\int_0^{\infty} W(y,z_k)F(y)dy = \sum_{i=1}^{K} W(z_i,z_k)F_i\Delta u_i, \quad \text{(A5)}$$

where $\Delta u_i = 0.5(\Delta z_i + \Delta z_{i+1})$.

For the cluster densities $C_k = F_k = F(z_k)$ in the equidistant mesh points $z_k = k \le N$, the convolution integral given by the second term in the right-hand-side of Eq. (A1) is evaluated using the original equation for discrete cluster sizes [Eq. (4)]. For cluster density in mesh points $z_k > N$, the convolution integral is estimated as follows:

$$\int_0^{z_k/2} W(y, z_k - y)F(y)F(z_k - y)dy = \sum_{i=1}^{m(k)-1} W(z_i, z_k - z_i)F_i\,F(z_k - z_i)\Delta u_i + R_k, \quad \text{(A6)}$$

where $m(k)$ is the index of the mesh point that satisfies the condition $z_{m(k)} \le z_k/2 < z_{m(k)+1}$. The remainder term R_k is given by

$$R_k = \frac{1}{2}Y_{m(k)}\Delta z_{m(k)} + \left[Y_{m(k)} + \frac{1}{2}\frac{Y_{m(k)+1} - Y_{m(k)}}{\Delta z_{m(k)+1}}\left(\frac{z_k}{2} - z_{m(k)}\right)\right] \times \left(\frac{z_k}{2} - z_{m(k)}\right), \quad \text{(A7)}$$

where $Y_i = W(z_i, z_k - z_i)F_i\,F(z_k - z_i)$; $i = m(k),\, m(k)+1$. To evaluate $W(z_i, z_k - z_i)$ and $F(z_k - z_i)$, we use the linear interpolation between two neighboring mesh points j and $j+1$, which satisfy the condition $z_j \le z_k - z_i \le z_{j+1}$.

Finally, the PSD evolution is described by the ODE set on the nonuniform mesh [Eq. (A3)]

$$\frac{dF_1}{d\tau} = -V\mu(D_1)F_1 - F_1\sum_{i=1}^{k} W(z_i,1)F_i\Delta u_i, \quad \text{(A8)}$$

$$\frac{dF_k}{d\tau} = -V\mu(D_k)F_k + \frac{1}{2}\sum_{i=1}^{k-1} W(i,k-i)F_iF_{k-i} - F_k\sum_{i=1}^{K} W(z_i,z_k)F_i\Delta u_i, \quad k \le N, \quad \text{(A9)}$$

$$\frac{dF_k}{d\tau} = -V\mu(D_{z_k})F_k + \sum_{i=1}^{m(k)-1} W(z_i, z_k - z_i) \times F_i F(z_k - z_i)\Delta u_i + R_k - F_k \sum_{i=1}^{K} W(z_i, z_k) F_i \Delta u_i, \quad N < k < K, \tag{A10}$$

$$\frac{dF_K}{d\tau} = 0. \tag{A11}$$

The initial value problem for this set can be solved by a standard numerical package. We use the RADAU code.[71] This code was developed for stiff and differential-algebraic problems and is based on the implicit Runge–Kutta method of variable order with an adaptive time-step control.

Direct comparison of the calculated PSDs and their moments to available analytical solutions of coagulation equations with simple kernels, $w_{ij} = \text{const}$, $w_{ij} = i + j$, and $w_{ij} = ij$, confirmed a very good performance of the numerical method described above. The detailed description of the numerical method will be presented elsewhere.

The coagulation equations were solved by the method described above with parameters listed in Tables I and II. Using mesh parameters $N = 100$ and $\varepsilon = 0.02$, the initial set of equations for PSD [Eqs. (3) and (4)] containing 10^7 equations (the equivalent radius of a spherical nanoparticle is 30 nm) was transformed into a set of about 700 equations. On a standard PC with central processing unit Intel(R) Core(TM) i5 2.67 GHz the solution time was about 40–100 s depending on input parameters.

[1] P. Moriarty, Rep. Prog. Phys. **64**, 297 (2001).
[2] A. Kumar, S. Kang, C. Larriba-Andaluz, H. Ouyang, C. J. Hogan, and R. M. Sankaran, Nanotechnology **25**, 385601 (2014).
[3] C. M. Sorensen and A. Chakrabarti, Soft Matter **7**, 2284 (2011).
[4] J. P. Liu, O. Gutfleisch, E. Fullerton, and D. Sellmyer, *Nanoscale Magnetic Materials and Applications* (Springer, New York, 2009).
[5] S. A. Claridge, A. W. Castleman, Jr., S. N. Khanna, C. B. Murray, A. Sen, and P. S. Weiss ACS Nano **3**, 244 (2009).
[6] J. A. Alonso, *Structure and Properties of Atomic Nanocluster* (Imperial College, London, 2011).
[7] H. Haberland, M. Karrais, M. Mall, and Y. Thurner, J. Vac. Sci. Technol., A **10**, 3266 (1992).
[8] H. Haberland, M. Mall, M. Moseler, Y. Qiang, T. Reiners, and Y. Thurner, J. Vac. Sci. Technol., A **12**, 2925 (1994).
[9] E. Barborini, P. Piseri, and P. Milani, J. Phys. D: Appl. Phys. **32**, L105 (1999).
[10] T. G. Dietz, M. A. Duncan, D. E. Powers, and R. E. Smalley, J. Phys. Chem. **74**, 6511 (1981).
[11] P. Milani and W. A. de Heer, Rev. Sci. Instrum. **61**, 1835 (1990).
[12] S. Maruyama, L. R. Anderson, and R. E. Smalley, Rev. Sci. Instrum. **61**, 3686 (1990).
[13] M. Tsuji, T. Seto, and Y. Otani, J. Nanopart. Res. **14**, 1 (2012).
[14] T. Seto, A. Inoue, H. Higashi, Y. Otani, M. Kohno, and M. Hirasawa, Carbon **70**, 224 (2014).
[15] S. G. Hall, M. B. Nielsen, A. W. Robinson, and R. E. Palmer, Rev. Sci. Instrum. **68**, 3335 (1997).
[16] H. R. Siekmann, Ch. Luder, J. Faehrmann, H. O. Lutz, and K.-H. Meiwes-Broer, Z. Phys. D **20**, 417 (1991).
[17] G. Ganteför, H. R. Siekmann, H. O. Lutz, and K. H. Meiwes-Broer, Chem. Phys. Lett. **165**, 293 (1990).
[18] R. P. Methling, V. Senz, D. Klinkenberg, T. Diederich, J. Tiggesbaumker, G. Holzhuter, J. Bansmann, and K. H. Meiwes-Broer, Eur. Phys. J. D **16**, 173 (2001).
[19] T. Lopez and L. Mangolini, J. Vac. Sci. Technol. B **32**, 061802 (2014).
[20] D. Mariotti and R. M. Sankaran, J. Phys. D **43**, 323001 (2010).
[21] P. Milani and S. Iannotta, Cluster Beam Synthesis of Nanostructured Materials (Springer, Berlin, 1999).
[22] J. Robertson, Mater. Sci. Eng. R **37**, 129 (2002).
[23] P. Roth, Proc. Combust. Inst. **31**, 1773 (2007).
[24] S. E. Pratsinis, Prog. Energy Combust. Sci. **24**, 197 (1998).
[25] M. S. Wooldridge, Prog. Energy Combust. Sci. **24**, 63 (1998).
[26] L. Madler, H. K. Kammler, R. Mueller, and S. E. Pratsinis, J. Aerosol Sci. **33**, 369 (2002).
[27] W. J. Stark and S. E. Pratsinis, Powder Technol. **126**, 103 (2002).
[28] D. E. Rosner, Ind. Eng. Chem. Res. **44**, 6045 (2005).
[29] R. Strobel and S. E. Pratsinis, J. Mater. Chem. **17**, 4743 (2007).
[30] M. K. Sharma, D. Qi, R. D. Buchner, W. J. Scharmach, V. Papavassiliou, and M. T. Swihart, ACS Appl. Mater. Interfaces **6**, 13542 (2014).
[31] T. T. Kodas and M. Hampden-Smith, *Aerosol Processing of Materials* (Wiley-VCH, New York, 1999).
[32] S. K. Friedlander, *Smoke, Dust and Haze: Fundamentals of Aerosol Dynamics*, 2nd ed. (Oxford University, New York, 2000).
[33] J. Musil, J. Vlcek, and P. Baroch, *Materials Surface Processing by Directed Energy Techniques*, edited by Y. Pauleau (Elsevier, New York, 2006), p. 67.
[34] G. Bräuer, B. Szyszka, M. Vergöhl, and R. Bandorf, Vacuum **84**, 1354 (2010).
[35] R. E. Palmer, S. Pratontep, and H. G. Boyen, Nat. Mater. **2**, 443 (2003).
[36] A. Benninghoven, Surf. Sci. **53**, 596 (1975).
[37] B. Chapman, *Glow Discharge Processes* (Wiley, New York, 1982).
[38] M. Ganeva, T. Peter, S. Bornholdt, H. Kersten, T. Strunskus, V. Zaporojtchenko, F. Faupel, and R. Hippler, Contrib. Plasma Phys. **52**, 881 (2012).
[39] B. Briehl and H. M. Urbassek, J. Vac. Sci. Technol., A **17**, 256 (1999).
[40] H. Mizuseki, Y. Jin, Y. Kawazoe, and L. T. Wille, Appl. Phys. A **73**, 731 (2001).
[41] P. Jensen, Rev. Mod. Phys. **71**, 1695 (1999).
[42] A. A. Turkin, M. V. Dutka, Y. T. Pei, D. I. Vainshtein, J. Th, and M. De Hosson, J. Appl. Phys. **111**, 124326 (2012).
[43] A. Garulli and F. Corticelli, Ultramicroscopy **34**, 299 (1990).
[44] K. Wasa, M. Kitabatake, and H. Adachi, *Thin Film Materials Technology Sputtering of Compound Materials* (Springer-Verlag, Berlin, 2004).
[45] B. M. Smirnov *et al.*, Europhys. Lett. **98**, 66005 (2012).
[46] D. Boldridge, Aerosol Sci. Technol. **44**, 182 (2010).
[47] P. Soille, *Morphological Image Analysis: Principles and Applications* (Springer-Verlag, New York, 2003).
[48] M. V. Smoluchowsky, Z. Phys. Chem. **92**, 129 (1917).
[49] A. M. Brasil, T. L. Farias, and M. G. Carvalho, J. Aerosol Sci. **30**, 1379 (1999).
[50] C. M. Sorensen, Aerosol Sci. Technol. **45**, 765 (2011).
[51] A. M. Brasil, T. L. Farias, and M. G. Carvalho, Aerosol Sci. Technol. **33**, 440 (2000).
[52] M. L. Eggersdorfer and S. E. Pratsinis, Aerosol Sci. Technol. **46**, 347 (2012).
[53] S. Vemury and S. E. Pratsinis, J. Aerosol Sci. **26**, 175 (1995).
[54] T. Matsoukas and S. K. Friedlander, J. Colloid Interface Sci. **146**, 495 (1991).
[55] M. K. Wu and S. K. Friedlander, J. Aerosol Sci. **24**, 273 (1993).
[56] L. Mädler and S. K. Friedlander, Aerosol Air Qual. Res. **7**, 304 (2007).
[57] T. Thajudeen, R. Gopalakrishnan, and C. J. Hogan, Aerosol Sci. Technol. **46**, 1174 (2012).
[58] M. Zurita-Gotor and D. E. Rosner, J. Colloid Interface Sci. **255**, 10 (2002).
[59] M. Zurita-Gotor and D. E. Rosner, J. Colloid Interface Sci. **274**, 502 (2004).
[60] N. A. Fuchs, *The Mechanics of Aerosols* (Macmillan, New York, 1964).
[61] R. Gopalakrishnan and C. J. Hogan, Phys. Rev. E **85**, 026410 (2012).
[62] H. Ouyang, R. Gopalakrishnan, and C. J. Hogan, J. Chem. Phys. **137**, 064316 (2012).
[63] D. L. Bunker, J. Chem. Phys. **32**, 1001 (1960).

[64]D. Ramkrishna, *Population Balances, Theory and Applications to Particulate Systems in Engineering* (Academic, New York, 2000).
[65]A. I. Roussos, A. H. Alexopoulos, and C. Kiparissides, Chem. Eng. Sci. **61**, 124 (2006).
[66]D. Mukherjee, A. Prakash, and M. R. Zachariah, J. Aerosol Sci. **37**, 1388 (2006).
[67]J. Kumar, "Numerical approximations of population balance equations in particulate systems," Ph.D. thesis (Otto-von-Guericke-University, Magdeburg, Germany, 2006).
[68]J. Kumar, M. Peglow, G. Warnecke, and S. Heinrich, Powder Technol. **182**, 81 (2008).
[69]V. Saliakas, C. Kotoulas, D. Meimaroglou, and C. Kiparissides, Can. J. Chem. Eng. **86**, 924 (2008).
[70]A. A. Turkin and A. S. Bakai, J. Nucl. Mater. **358**, 10 (2006).
[71]E. Hairer and G. Wanner, *Solving Ordinary Differential Equations II. Stiff and Differential-Algebraic Problems*, Springer Series in Computational Mathematics Vol. 14 (Springer-Verlag, New York, 1996).